ACS APPLIED MATERIALS & INTERFACES

www.acsami.org

Research Article

Ultrastable $CsPbBr_3$@$CsPb_2Br_5$@TiO_2 Composites for Photocatalytic and White Light-Emitting Diodes

Chen Zhang, Zeyu Wang, Minqiang Wang,* Jindou Shi, Junnan Wang, Zheyuan Da, Yun Zhou, Youlong Xu, Nikolai V. Gaponenko, and Arshad Saleem Bhatti

Cite This: *ACS Appl. Mater. Interfaces* 2023, 15, 35216−35226

Read Online

ACCESS | Metrics & More | Article Recommendations | Supporting Information

ABSTRACT: Although cesium halide lead ($CsPbX_3$, X = Cl, Br, I) perovskite quantum dots (QDs) have excellent photovoltaic properties, their unstable characteristics are major limitations to application. Previous research has demonstrated that the core−shell structure can significantly improve the stability of $CsPbX_3$ QDs and form heterojunctions at interfaces, enabling multifunctionalization of perovskite materials. In this article, we propose a convenient method to construct core−shell-structured perovskite materials, in which $CsPbBr_3$@$CsPb_2Br_5$ core−shell micrometer crystals can be prepared by controlling the ratio of Cs^+/Pb^{2+} in the precursor and the reaction time. The materials exhibited enhanced optical properties and stability that provided for further postprocessing. Subsequently, $CsPbBr_3$@$CsPb_2Br_5$@TiO_2 composites were obtained by coating a layer of dense TiO_2 nanoparticles on the surfaces of micrometer crystals through hydrolysis of titanium precursors. According to density functional theory (DFT) calculations and experimental results, the presence of surface TiO_2 promoted delocalization of photogenerated electrons and holes, enabling the $CsPbBr_3$@$CsPb_2Br_5$@TiO_2 composites to exhibit excellent performance in the field of photocatalysis. In addition, due to passivation of surface defects by $CsPb_2Br_5$ and TiO_2 shells, the luminous intensity of white light-emitting diodes prepared with the materials only decayed by 2%−3% at high temperatures (>100 °C) when working for 24 h.

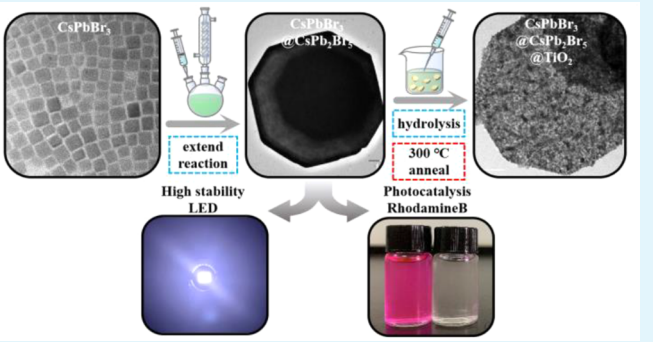

KEYWORDS: *Perovskites, Composites, Anatase TiO_2, Photocatalysis, Optoelectronic devices*

INTRODUCTION

Cesium halide lead perovskite ($CsPbX_3$ (X = Cl, Br, I)) quantum dots (QDs) have great potential in photovoltaics due to their harmonizable band gap and high photon-to-electron conversion efficiency.[1−3] Among them, the excellent light absorption and charge transfer properties have attracted much attention in fields of solar cells and photocatalysis,[4−6] and the high photoluminescence quantum yield (PLQY) was considered as one of the most promising materials for display and illumination.[7−10] However, the excellent optoelectronic characteristics of $CsPbX_3$ QDs are often overshadowed by disadvantages associated with their instability.[11−14] Therefore, a great deal of work has been devoted to improving the stability of perovskite $CsPbX_3$ QDs. There were three main directions: (1) construction of core−shell structures, (2) modification of surfaces using ligands, and (3) packaging by polymers. Among them, core−shell-structured perovskite QDs were an important class of nanomaterials, which not only used stable substances as protective shells to directly isolate QDs from PL quenching molecules, but also formed heterojunctions at interfaces, providing a platform for exploring completely new photophysical properties.[15−17]

Generally, there were two mainstream schemes for the formation of a core−shell structure of perovskite $CsPbX_3$ as follows. First, heterogeneous shells were epitaxially grown on the $CsPbX_3$ nanocrystal surfaces. For example, Jiang et al. used polyethylenimine as a ligand to promote the conversion of $CsPbBr_3$ to $CsPb_2Br_5$ by grinding and obtained $CsPbBr_3$/$CsPb_2Br_5$ nanocrystals with a core−shell structure, which improved the stability of the products.[18] Baek et al. prepared $CsPbBr_3$@Cs_4PbBr_6 nanocomposites by embedding $CsPbBr_3$ into Cs_4PbBr_6 substrates by a mechanochemical method.[19] In addition, heterogeneous shells such as TiO_2,[20] $NaYF_4$,[21] and $PbBr_2$[22] were epitaxially grown. Such strategies were usually effective in passivating the surface defects of $CsPbX_3$ nanocrystals and isolating them sufficiently from the external environment but also often led to dissolution of exposed

Received: May 17, 2023
Accepted: July 11, 2023
Published: July 16, 2023

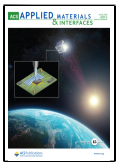

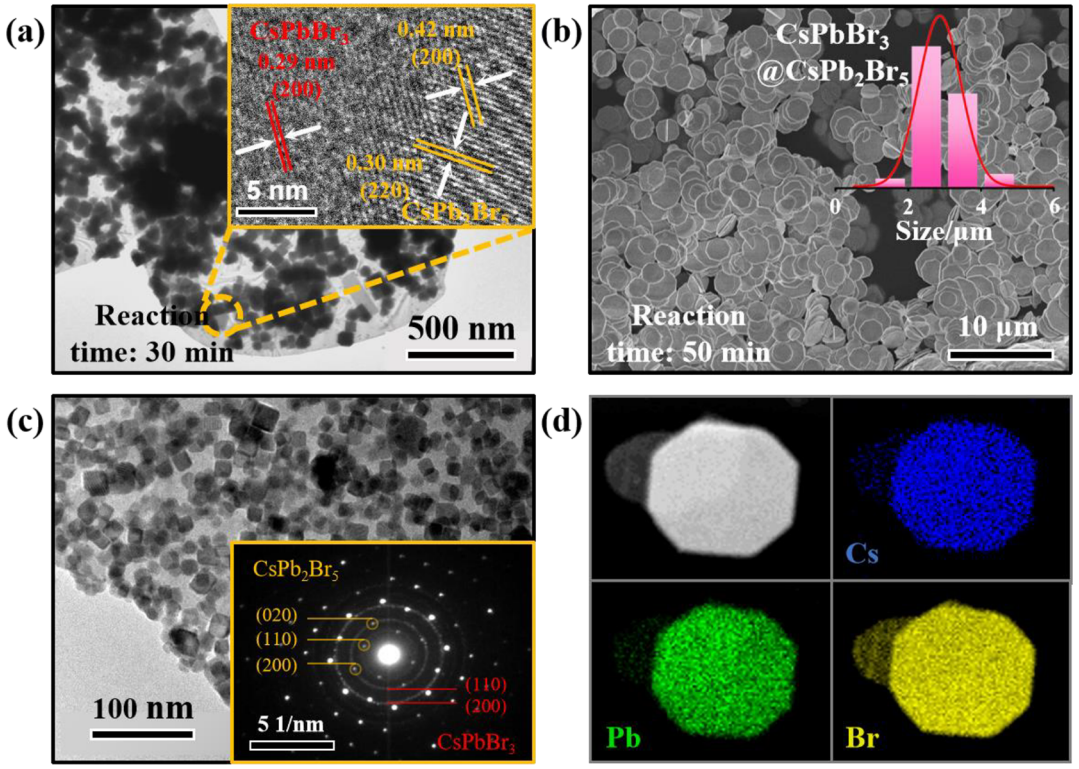

Figure 1. After Cs-OA injection: (a) TEM image of the reaction for 30 min and (b) SEM image of the reaction for 50 min. Panel (a) inset shows the HRTEM image at yellow circle. Panel (b) inset shows the size distribution of $CsPbBr_3$@$CsPb_2Br_5$ micrometer crystals. (c) After 50 min of reaction, TEM image of $CsPbBr_3$@$CsPb_2Br_5$ micrometer crystals. The inset is SAED image of a single micrometer crystal. (d) EDS spectra of $CsPbBr_3$@$CsPb_2Br_5$ micrometer crystals.

nanocrystals during the coating process. Therefore, it was a great challenge to adopt mild growth methods to make nanocrystals retain their original crystal structure. Second, hollow or mesoporous materials (generally at submicrometer scale) are used to package $CsPbX_3$ nanocrystals. For example, Xie et al. preprepared hollow SiO_2 spheres as protective shells and then grew $CsPbBr_3$/$CsPb_2Br_5$ composites on their interior.[23] Tong et al. encapsulated $CsPbBr_3$ nanocrystals in the pores of zeolite resulting in $CsPbX_3$@zeolite with high quantum yields and showing excellent thermal/optical stability.[24] However, water/oxygen molecules and heat would undergo the same process for diffusion,[25] resulting in $CsPbX_3$ nanocrystals failing to completely insulate surroundings. Moreover, since $CsPbX_3$ nanocrystals were free inside cavities, they failed to make close contact with heterogeneous shell and also failed to form high-quality heterojunctions at interfaces.[26−28] Therefore, it is necessary to develop a convenient synthesis strategy that can preserve the original structure and optical properties of $CsPbX_3$ QDs while enabling them to form heterojunctions with epitaxial substrates to expand the applications of perovskite materials.

Herein, we propose a facile preparation scheme for the construction of core−shell-structured $CsPbBr_3$ QDs. Through controlling the ratio of halide salts and reaction time, a series of uniform $CsPbBr_3$@$CsPb_2Br_5$ octagonal core−shell micrometer crystals were prepared by epitaxial growth of $CsPb_2Br_5$ on the $CsPbBr_3$ surface. Benefiting from passivation of surface defects by $CsPb_2Br_5$ shells, the materials exhibited enhanced optical properties and water/thermal stability, laying the foundation for further post-treatment to achieve multifunctionalization of perovskite materials. Subsequently, a layer of dense TiO_2 nanoparticles was encapsulated on the surfaces of $CsPbBr_3$@$CsPb_2Br_5$ core−shell micrometer crystals by hydrolyzing tetrabutyl titanate (TBOT). This strategy not only avoided crystal structure decomposition caused by direct processing of naked $CsPbBr_3$ QDs, but also combined the excellent light absorption effect of QDs with the clean catalytic performance of TiO_2, expanding the application of QDs in photocatalysis. Meanwhile, due to long-term stability and lower density of defect states, the materials were also attractive for display applications, and prepared quasi-white LEDs exhibited surprising sustained operating stability at high temperatures (>100 °C).

RESULTS AND DISCUSSION

Crystal Structure and Optical Properties of $CsPbBr_3$@$CsPb_2Br_5$ Core−Shell Micrometer Crystals. $CsPbBr_3$@$CsPb_2Br_5$ core−shell micrometer crystals could be obtained simply by holding a reaction for 50 min after Cs-OA injection through the traditional thermal injection method. To demonstrate that the reaction time was the determining factor in obtaining core−shell structures, samples with different reaction times were observed by transmission electron microscopy (TEM) and scanning electron microscopy (SEM). First, the sample was pure $CsPbBr_3$ QDs when the reaction time was 5 s (Figure S1a). When the time was extended to 30 min, it was clearly seen that a crystal shell appeared at the periphery of QDs, completely encasing $CsPbBr_3$ (Figure 1a). The high-resolution transmission electron microscopy (HRTEM) image shown in the inset also has two different lattice fringes corresponding to cubic $CsPbBr_3$ (0.29 nm (200) crystal plane) and tetragonal

https://doi.org/10.1021/acsami.3c07081
ACS Appl. Mater. Interfaces 2023, 15, 35216−35226

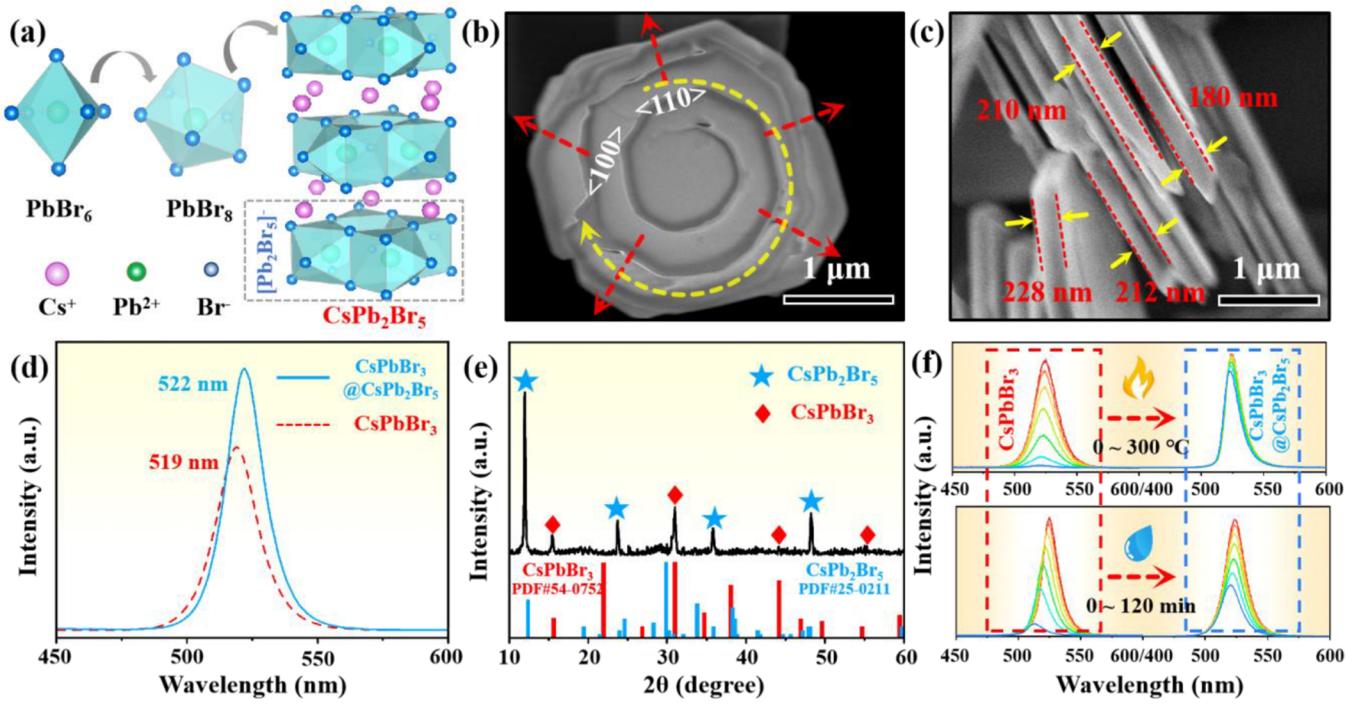

Figure 2. (a) Schematic diagram of crystal structure and formation process of $CsPb_2Br_5$. (b) SEM pictures of surface of partial $CsPbBr_3$@$CsPb_2Br_5$ micrometer crystals. (c) SEM pictures of cross-section of $CsPbBr_3$@$CsPb_2Br_5$ micrometer crystals. (d) PL spectra (λ_{em} = 365 nm), (e) XRD patterns, and (f) water/thermal stability comparison of $CsPbBr_3$@$CsPb_2Br_5$ micrometer crystals.

$CsPb_2Br_5$ (0.30 nm (220), 0.42 nm (200) crystal planes). Further, when the reaction time reached 50 min, SEM (Figure 1b) and TEM (Figure S1b) observed that $CsPbBr_3$ QDs had disappeared, and a large number of octagonal micrometer crystals with smooth surfaces were formed. The grain size of the materials was approximately 2.7 μm and had good dispersion; presumably all QDs were encapsulated inside $CsPb_2Br_5$ at this time. The magnified TEM images confirmed this, with a large number of $CsPbBr_3$ QDs (sizes about 14−17 nm) embedded inside the micrometer crystals and still retaining the original cubic morphology without agglomeration or dissolution (Figure 1c). The inset shows selected electron diffraction (SAED) images of individual micrometer crystals indicating the $CsPb_2Br_5$ substrate as typical monocrystal diffraction spots and internal $CsPbBr_3$ QDs as ring-like polycrystalline fringes, both of which had excellent crystallinity. The XRD results were also consistent with this. The $CsPbBr_3$@$CsPb_2Br_5$ micrometer crystals reacting for 50 min had sharp diffraction peaks (Figure S1c), but when reaction time was further extended to 90 min, $CsPbBr_3$ diffraction peaks almost disappeared, which was attributed to gradual transformation of product to pure phase $CsPb_2Br_5$ due to a prolonged high temperature environment. The corresponding energy dispersive spectroscopy (EDS) showed uniform distribution of Cs, Pb, and Br elements in octagonal micrometer crystals with a ratio of 1:1.8:4.7 (Figure 1d, Figure S2). In short, it was demonstrated by TEM and SEM observations that homogeneous $CsPbBr_3$@$CsPb_2Br_5$ core−shell micrometer crystals could be obtained by simply controlling the reaction time.

By investigating the solution system and crystal structure, we explained the formation of $CsPbBr_3$@$CsPb_2Br_5$ octagonal micrometer crystals. First, induced formation of $CsPb_2Br_5$ was carried out by excess $PbBr_2$ in a precursor solution. This reaction system would lead to insufficient binding of Pb^{2+} and Br^- to Cs^+ in solution when Cs^+ was introduced and formation of $[Pb_2Br_5]^-$ complexes due to action of long-chain ligands (oleic acid and oleylamine).[29] As the system balanced, the lead halide complex reorganized in solution to form $CsPb_2Br_5$ nanoparticles, which can be summarized as the following reactions:

$$PbBr_2 + [PbBr_3]^- \rightarrow [Pb_2Br_5]^- \quad (1)$$

$$Cs^+ + [Pb_2Br_5]^- \rightarrow CsPb_2Br_5 \quad (2)$$

Subsequently, since the lattice mismatch between $CsPbBr_3$ and $CsPb_2Br_5$ was less than 3%,[30] and the two formed composites with lower overall energy,[31] $CsPb_2Br_5$ would tend to be on $CsPbBr_3$ surface epitaxial growth instead of being individually present in solution. By precise control of reaction time, we could not only retain the cubic morphology and monodispersity of QDs, but also formed the $CsPb_2Br_5$ shell on their surfaces. Further, all micrometer crystals maintained a uniform octagonal shape due to the inherent symmetry of the $CsPb_2Br_5$ crystal structure.[32] As shown in Figure 2a, $CsPbBr_3$ QDs preferentially formed a PbBr6 octahedral structure during growth, but under the effect of thermodynamics and a Pb-rich environment, the $PbBr_6$ octahedron would break, allowing Pb^{2+} and Br^- ions to embed into an octahedron, forming a $PbBr_8$ polyhedron consisting of a trigonal prism and two lateral top corners.[33,34] Then, the $PbBr_8$ polyhedra shared top-angle Br atoms with each other, forming a tetragonal phase $[Pb_2Br_5]^-$ layer, and further combined with Cs^+ ions to form the crystal structure of $CsPb_2Br_5$. Therefore, from an overall perspective, since the structure of $CsPb_2Br_5$ was a sandwich structure consisting of a tetragonal phase $[Pb_2Br_5]^-$ layer and Cs^+ layer, which differed from the three-dimensional linkage structure of cubic perovskite $CsPbBr_3$, it would lead to easier

https://doi.org/10.1021/acsami.3c07081
ACS Appl. Mater. Interfaces 2023, 15, 35216−35226

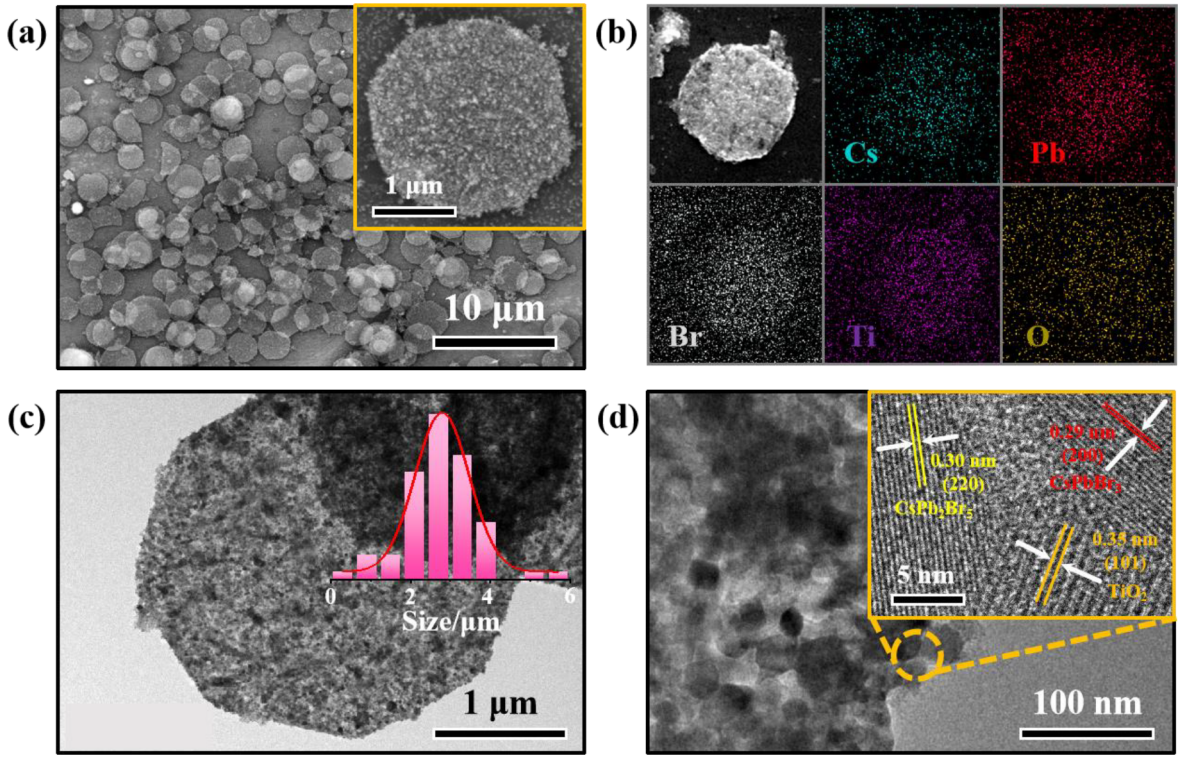

Figure 3. (a) SEM images, (b) EDS spectra, (c) TEM image (inset shows size distribution of $CsPbBr_3$@$CsPb_2Br_5$@TiO_2), and (d) HRTEM image of $CsPbBr_3$@$CsPb_2Br_5$@TiO_2 composites.

lateral growth of $CsPb_2Br_5$ along two dimensions.[32,35] According to the HRTEM test results (Figure 1a), (220) and (200) faces of $CsPb_2Br_5$ were exposed during lateral growth, allowing them to grow in ⟨100⟩ and ⟨110⟩ two different directions (with an angle of 135°) (Figure 2b).[33] Due to limitation of the solution system, both directions maintained the same rate of gradual outward diffusion, eventually resulting in all micrometer crystals showing uniform octagonal shapes. Further, the presence of $CsPbBr_3$@$CsPb_2Br_5$ micrometer crystals with different thicknesses indicated that the materials also had a certain growth rate in the vertical direction (Figure 2c). Moreover, a series of helical stripes exist on the surface of partial micrometer crystals (Figure 2b), demonstrating that the growth process of the grains in the vertical direction was not simply a uniform diffusion, but a gradual aggregation along helical direction, and this might be caused by the unique molecular dynamics and Coulomb forces between $CsPbBr_3$ and $CsPb_2Br_5$.[31] Finally, due to the limitation of the $CsPb_2Br_5$ layered crystal structure, the growth rate in the vertical direction was much lower than lateral growth, which resulted in all micrometer crystals being octagonal and thin-plate shaped.

Subsequently, we investigated optical properties of $CsPbBr_3$@$CsPb_2Br_5$ micrometer crystals. The corresponding PL spectra are shown in Figure 2d, with the micrometer crystal emission peak at 522 nm and pure $CsPbBr_3$ QDs at 519 nm. The close peak position indicated that both of them had the same emission source, and the slight redshift was attributed to the increase of QDs core size due to the long-time high temperature environment. Further, $CsPbBr_3$@$CsPb_2Br_5$ micrometer crystals exhibited enhanced fluorescence intensity with quantum yields (QY) of 83% ($CsPbBr_3$ QDs 55%) and narrower full width at half maximum (fwhm) ($CsPbBr_3$@$CsPb_2Br_5$ 16 nm, $CsPbBr_3$ QDs 19 nm). Previous studies had confirmed that dangling bonds and halide vacancies of $CsPbBr_3$ QDs were nonradiative recombination centers and generated structural defects in the band gap.[18,31] Therefore, reducing the density of these defects is essential for high-performance carrier transport. Since the $CsPb_2Br_5$ shell grew epitaxially on the surfaces of QDs, it could effectively fill the dangling bonds and halide vacancies improving the radiation recombination rate. As a result, micrometer crystals showed higher PLQY than pure QDs. The XRD results also demonstrated that the micrometer crystals consisted of $CsPb_2Br_5$ and $CsPbBr_3$ with no other impurity phases produced (Figure 2e). Finally, we tested the stability of $CsPbBr_3$@$CsPb_2Br_5$ micrometer crystals under high temperature and water environments (Figure 2f). After annealing at 0−300 °C for 1 h, the fluorescence intensity of $CsPbBr_3$ QDs decayed substantially until it almost disappeared, but $CsPbBr_3$@$CsPb_2Br_5$ could still retain more than 80% of the fluorescence intensity. Water stability showed similar results, with the fluorescence intensity of $CsPbBr_3$ QDs remaining only 10% of the initial intensity after 120 min, while $CsPbBr_3$@$CsPb_2Br_5$ remained above 45%. Both stability test results demonstrated that the stability of the $CsPbBr_3$ QDs was substantially improved after $CsPb_2Br_5$ shell passivation, providing a basis for further packaging of TiO_2 nanoparticles.

Crystal Structure and Optical Properties of $CsPbBr_3$@$CsPb_2Br_5$@TiO_2 Composites. Although the water/thermal stability of $CsPbBr_3$ QDs packaged in $CsPb_2Br_5$ had been significantly improved, it was not sufficient for harsh environmental erosion faced by practical applications. Through hydrolysis and annealing of tetrabutyl titanate (TBOT), we continued to encapsulate a TiO_2 shell on the surfaces of $CsPbBr_3$@$CsPb_2Br_5$ micrometer crystals, which combined the

https://doi.org/10.1021/acsami.3c07081
ACS Appl. Mater. Interfaces 2023, 15, 35216−35226

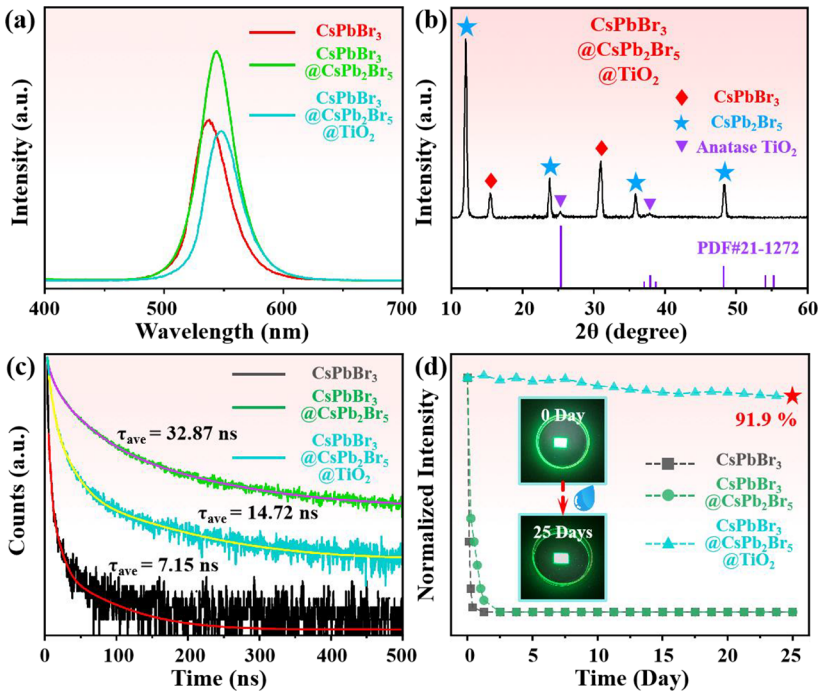

Figure 4. (a) Comparison of PL spectra (λ_{em} = 365 nm). (b) XRD patterns of $CsPbBr_3$@$CsPb_2Br_5$@TiO_2 composites. (c) Time-resolved fluorescence spectra. (d) Water stability comparison of $CsPbBr_3$ QDs, $CsPbBr_3$@$CsPb_2Br_5$ micrometer crystals, and $CsPbBr_3$@$CsPb_2Br_5$@TiO_2 composites. The inset shows sample images of $CsPbBr_3$@$CsPb_2Br_5$@TiO_2 composites before and after 25 days of immersion in water.

clean photocatalytic properties of TiO_2 with the excellent light absorption properties of perovskite QDs, in addition to further improving their stability. The process is shown in Figure S3a; after TiO_2 encapsulation, the original smooth surfaces of $CsPbBr_3$@$CsPb_2Br_5$ micrometer crystals were wrapped by tiny TiO_2 particles, forming a dense and uniform TiO_2 shell. SEM images at low magnification showed that $CsPbBr_3$@$CsPb_2Br_5$@TiO_2 composites still retained the original octagonal morphology with an average size of about 3.1 μm (Figure 3c) and had uniform size and good dispersion (Figure 3a). As a comparison, we prepared $CsPbBr_3$@TiO_2 composites using the same procedure (Figure S3b). Lacking a $CsPb_2Br_5$ layer protection, the fluorescence intensity of $CsPbBr_3$@TiO_2 composites decayed dramatically, especially after high-temperature annealing; the fluorescence of this powder was already hardly detectable, proving that the $CsPb_2Br_5$ layer played a crucial role. Subsequently, EDS spectra showed that both Ti and O were homogeneously distributed on the surfaces of $CsPbBr_3$@$CsPb_2Br_5$ micrometer crystals, forming a uniform shell layer (Figure 3b). Further, both TEM and HRTEM observed a layer of tiny TiO_2 particles (about 20−30 nm) attached to micrometer crystal surfaces, and samples also had three lattice fringes with different spacings corresponding to cubic $CsPbBr_3$ QDs (0.29 nm (200) crystal plane), tetragonal $CsPb_2Br_5$ (0.30 nm (220) crystal plane), and anatase TiO_2 (0.35 nm (101) crystal plane) (Figure 3c, d). In addition, we also investigated the effect of different TBOT additions on $CsPbBr_3$@$CsPb_2Br_5$ micrometer crystals. The results showed that too little (5 μL) TBOT would lead to TiO_2 particles free in solution (Figure S4a), failing to fully fill the surfaces of micrometer crystals. However, too much (20 μL) TBOT would lead to decomposition of $CsPbBr_3$@$CsPb_2Br_5$ (Figure S4b), which then agglomerated into flakes. Therefore, the proper ratio of TBOT to water is very important.

Further, we tested the optical properties of $CsPbBr_3$@$CsPb_2Br_5$@TiO_2 composites. First, the PL spectra showed the emission peak of $CsPbBr_3$@$CsPb_2Br_5$@TiO_2 composites with a wavelength of 524 nm and fwhm of 18 nm, which were consistent with the characteristics of $CsPbBr_3$ QDs (Figure 4a). The slight redshift might be caused by the diffusion of the wave functions of electrons and holes into the shell layer.[44] Subsequently, the absorption spectra showed that both $CsPbBr_3$@$CsPb_2Br_5$ and $CsPbBr_3$@$CsPb_2Br_5$@TiO_2 showed increased absorbance in the range of 300−400 nm, attributed to the UV activity of $CsPb_2Br_5$ and TiO_2 surface layers (Figure S5). Moreover, the light absorption ability of $CsPbBr_3$@$CsPb_2Br_5$@TiO_2 was also increased to 550−700 nm, which was caused by amorphous TiO_2 and carbon residues. The corresponding XRD patterns indicated slight anatase TiO_2 diffraction peaks in addition to diffraction peaks of $CsPbBr_3$ and $CsPb_2Br_5$, which were attributed to low annealing temperatures that did not make TiO_2 fully crystallize (Figure 4b). Although the intensity of the diffraction peaks of TiO_2 was low, it did not affect our confirmation of the completed composite of $CsPbBr_3$, $CsPb_2Br_5$, and TiO_2. Further, the average lifetimes of $CsPbBr_3$ (519 nm), $CsPbBr_3$@$CsPb_2Br_5$ (522 nm), and $CsPbBr_3$@$CsPb_2Br_5$@TiO_2 (524 nm) were monitored, respectively. The results in Figure 4c show that the average lifetimes of $CsPbBr_3$ QDs were 7.15 ns, $CsPbBr_3$@$CsPb_2Br_5$ micrometer crystals were 32.87 ns, and $CsPbBr_3$@$CsPb_2Br_5$@TiO_2 composites were 14.72 ns. Among them, $CsPbBr_3$@$CsPb_2Br_5$ had the longest decay lifetime, indicating that the $CsPb_2Br_5$ shell passivated the nonradiative decay process of $CsPbBr_3$ QDs, increasing the radiative recombination rate of carriers. While after TiO_2 passivation, the fluorescence intensity and lifetime of micrometer crystals were reduced, indicating that carriers were efficiently separated in this system, which may be related to the unique energy band structure of this ternary composites, as discussed in subsequent

https://doi.org/10.1021/acsami.3c07081
ACS Appl. Mater. Interfaces 2023, 15, 35216−35226

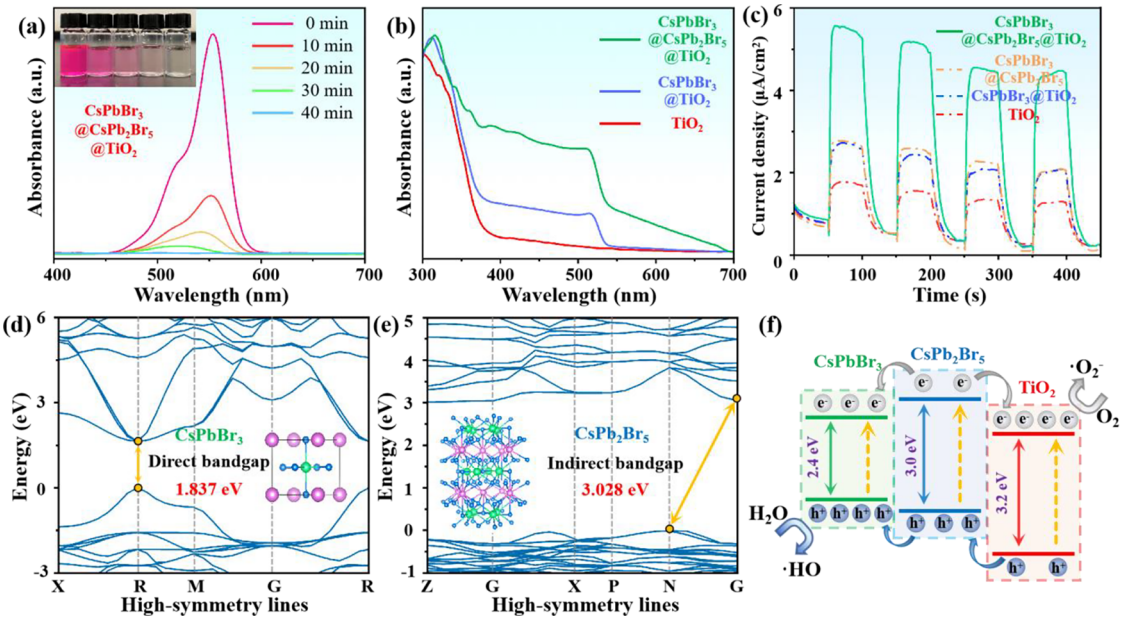

Figure 5. (a) UV−vis absorption spectra of $CsPbBr_3$@$CsPb_2Br_5$@TiO_2 composites for degradation of RhB. The photocatalytic light source was a 500 W Xe lamp with an AM 1.5 G filter. Comparison of (b) UV−vis absorption spectra and (c) chopped photocurrent response (0.1 M Na_2SO_4) of $CsPbBr_3$@$CsPb_2Br_5$@TiO_2. Using density functional theory (DFT), the electronic structures of (d) cubic $CsPbBr_3$ and (e) tetragonal $CsPb_2Br_5$ were calculated. (f) Energy band diagrams of the $CsPbBr_3$@$CsPb_2Br_5$@TiO_2 composites.

sections on photocatalysis. Finally, we tested the water stability of all three to ensure that materials could be used in aqueous systems for photocatalytic applications (Figure 4d). The results showed that $CsPbBr_3$ QDs were completely quenched after 5 h of immersion, benefiting from the protective effect with the external hydrophobic long-chain ligands. After 14 h of immersion, $CsPbBr_3$@$CsPb_2Br_5$ was completely quenched, attributed to external $CsPb_2Br_5$ decomposing first into $CsPbBr_3$ and $PbBr_2$ when exposed to water, acting as buffer, according to the following equation:[34]

$$CsPb_2Br_5 \xrightarrow{H_2O} Pb^{2+} + 2Br^- + CsPbBr_3 \quad (3)$$

In stark contrast, $CsPbBr_3$@$CsPb_2Br_5$@TiO_2 composites maintained PL strength of more than 90% even after 25 days of immersion.

Photocatalytic Performance of $CsPbBr_3$@$CsPb_2Br_5$@TiO_2 Composites. We evaluated the photocatalytic effect of the material by degrading dye in aqueous environments, using rhodamine-B (RhB) as a representative of organic pollutants. In contrast, the catalytic processes of three materials, $CsPbBr_3$@$CsPb_2Br_5$@TiO_2, $CsPbBr_3$@TiO_2, and pure TiO_2, were recorded with the following results: $CsPbBr_3$@$CsPb_2Br_5$@TiO_2 degraded 98.7% after 40 min (Figure 5a). $CsPbBr_3$@TiO_2 degraded 87.4% after 90 min (Figure S6a). Pure TiO_2 degraded only 79.9% after 16 h (Figure S6b). Thus, it was found that $CsPbBr_3$@$CsPb_2Br_5$@TiO_2 composites had the best photocatalytic performance. We speculated that the first reason was the excellent visible light absorption of in-shell $CsPbBr_3$ QDs. Therefore, the UV−vis absorption spectra of the three materials were tested (Figure 5b). The results showed that both $CsPbBr_3$@$CsPb_2Br_5$@TiO_2 and $CsPbBr_3$@TiO_2 exhibited an absorption edge near 520 nm, which was consistent with the absorption position of the $CsPbBr_3$ core. However, $CsPbBr_3$@$CsPb_2Br_5$@TiO_2 composites had higher absorption intensity, attributed to the shells of stable $CsPb_2Br_5$ protecting exposed QDs during the postprocessing process, so that the final product still had superior visible light absorption properties. For the $CsPbBr_3$@TiO_2 composite, a weaker absorption intensity was exhibited between 500 and 550 nm due to massive decomposition of $CsPbBr_3$. Pure TiO_2, with a wide band gap (3.2 eV), only absorbed the UV light before 400 nm, and a large amount of optical resources were wasted.[36,37] It could be determined from the above analysis of light absorption angles that $CsPbBr_3$ QDs cores extended the light utilization range up to 550 nm, while $CsPb_2Br_5$ and TiO_2 shells enhanced UV light absorption; thus, $CsPbBr_3$@$CsPb_2Br_5$@TiO_2 composites had the highest photocatalytic efficiency. The second reason was attributed to higher carrier transport efficiency inside $CsPbBr_3$@$CsPb_2Br_5$@TiO_2 composites, as evidenced by chopped photocurrent response, and the results are shown in Figure 5c. All samples exhibited a highly stable photoresponse, but the photocurrent of $CsPbBr_3$@$CsPb_2Br_5$@TiO_2 was significantly higher than other materials. The higher photocurrent indicated that charge transfer resistance of the material was markedly reduced, demonstrating that introduction of TiO_2 nanoparticles promoted internal carrier transport.[38] Furthermore, the tiny grains could spatially limit exciton diffusion length, improving photocurrent efficiency. In this paper, TiO_2 particles attached to $CsPbBr_3$@$CsPb_2Br_5$ micrometer crystals were only 20−30 nm (Figure 3d), which enabled carriers to diffuse efficiently through surface TiO_2 shell, enhancing electron and hole transport efficiency.

Further, we analyzed the mechanism of photocatalytic reaction of $CsPbBr_3$@$CsPb_2Br_5$@TiO_2 composites from an energy band perspective. First, the electronic structures of cubic $CsPbBr_3$ and tetragonal $CsPb_2Br_5$ were calculated by density functional theory (DFT) (Figure 5d, e). The results showed that cubic phase $CsPbBr_3$ was a direct band gap semiconductor with a band gap of 1.837 eV, and tetragonal $CsPb_2Br_5$ was an indirect band gap semiconductor with a band gap of 3.028 eV. Both simulations agreed with our experimental dates ($CsPbBr_3$ 2.361 eV, $CsPb_2Br_5$ 3.019 eV)

https://doi.org/10.1021/acsami.3c07081
ACS Appl. Mater. Interfaces 2023, 15, 35216−35226

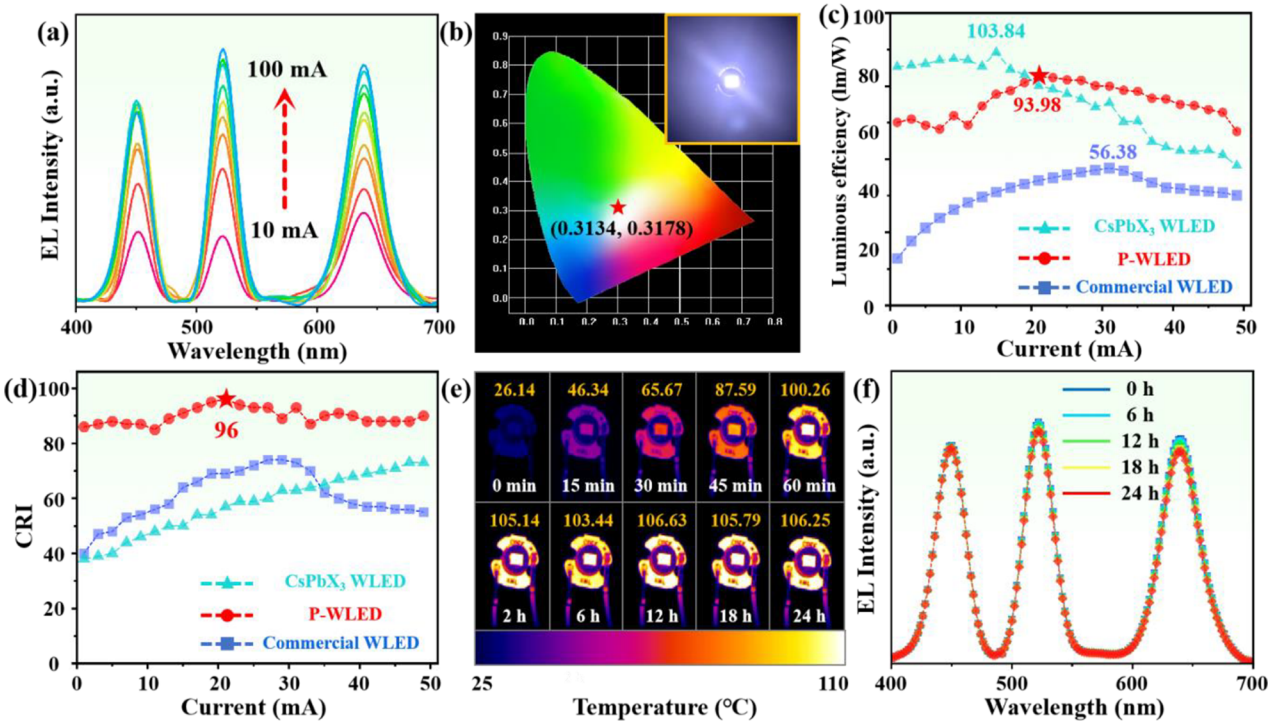

Figure 6. (a) EL spectra of P-WLED at 10−100 mA drive current. (b) CIE coordinates of P-WLED at 20 mA drive current. Inset shows electroluminescence photograph of P-WLED. Comparison of (c) luminous efficiency and (d) color rendering index of P-WLEDs. (e) Surface temperature (yellow numbers represent the surface temperature of P-LED (in °C)). (f) EL spectrum of P-WLED after 24 h of continuous operation at 21 mA drive current.

(Figure S7). The character of the indirect band gap proved that the $CsPb_2Br_5$ shell had non-PL activity, and emitting sources were $CsPbBr_3$ QDs. According to previous reports, the work functions of cubic $CsPbBr_3$, tetragonal $CsPb_2Br_5$, and anatase TiO_2 were about 4.65, 4.86, and 5.94 eV,[30,39,40] respectively, which led to the energy band structure of the composites as shown in Figure 5f. The results showed that a typical type-I heterojunction was formed between $CsPbBr_3$ and $CsPb_2Br_5$, and a typical type-II heterojunction was formed between $CsPb_2Br_5$ and TiO_2. When high-energy light irradiated $CsPbBr_3$@$CsPb_2Br_5$@TiO_2, electrons in valence bands of $CsPbBr_3$, $CsPb_2Br_5$, and TiO_2 were excited and jumped to conduction bands to produce photoelectrons (e^-) and left corresponding photoholes (h^+) in valence bands. Since the valence band potential of $CsPbBr_3$ had the strongest attraction effect on holes, both holes on valence bands of $CsPb_2Br_5$ and TiO_2 were transferred to $CsPbBr_3$, causing holes to separate from $CsPb_2Br_5$ and TiO_2. Similarly, due to the most negative conduction band potential of TiO_2, photoelectrons on the conduction band of $CsPb_2Br_5$ would be preferentially transferred to TiO_2. At this time, the TiO_2 conduction band collected most electrons and then reacted with O_2 to form superoxide radicals ($\cdot O_2^-$); the $CsPbBr_3$ valence band collected all holes and then reacted with H_2O to form hydroxyl radicals (·OH). Photoelectrons and holes achieved the maximum separation in this system, promoting the efficiency of photocatalytic degradation of organic pollutants. As evidenced by time-resolved PL spectra previously described (Figure 4c), $CsPb_2Br_5$ shells extend the PL decay lifetime of $CsPbBr_3$ QDs by more than four times (from 7.15 to 32.87 ns), demonstrating the formation of type-I heterojunctions between the two, facilitating exciton recombination on $CsPbBr_3$ QDs. The introduction of TiO_2 resulted in a significant reduction in the $CsPbBr_3$@$CsPb_2Br_5$ micrometer crystal lifetime (from 32.87 to 14.72 ns), implying that TiO_2 acted as an electron acceptor promoting electron transfer to its own conduction band and hole delocalization, resulting in lower radiative recombination.

Finally, we tested the stability of these materials after multiple cycles of catalysis (Figure S8). The results showed that $CsPbBr_3$@$CsPb_2Br_5$@TiO_2 composites could maintain more than 95% degradation efficiency within 40 min even after 10 cycles of experiments, demonstrating an excellent reusability performance. On the contrary, the efficiency of $CsPbBr_3$@TiO_2 composites was only 31.6% after the same process, proving that the high defect density inherent in QDs would further promote decomposition of $CsPbBr_3$ under environmental erosion after the absence of $CsPb_2Br_5$ protection, which severely deteriorated catalytic efficiency.

Optical Properties of WLED. Compared to pure $CsPbBr_3$ QDs, although the PL intensity of $CsPbBr_3$@$CsPb_2Br_5$@TiO_2 composites was slightly reduced (due to decomposition of exposed QDs and the energy band structure promoting electron−hole separation), they were still one of the potential candidates in fields for displays, and illumination attributed to their lower defect density and long-term water/thermal stability.[41] We prepared $CsPb(Br/I)_3$@$CsPb_2(Br/I)_5$@TiO_2 as a red light source by the anion exchange method (PL peak position 640 nm, Figure S9). Then, the material and $CsPbBr_3$@$CsPb_2Br_5$@TiO_2 were encapsulated in polymer films and integrated on 450 nm blue light chips to assemble a quasi-perovskite white light-emitting diode (referred to as P-WLED). Similarly, as a comparison, we also prepared $CsPbX_3$ WLEDs without shell passivation by the same polymer encapsulation strategy. Figure 6a exhibits the electroluminescence (EL) spectra of P-WLED at 10 to 100 mA drive current.

https://doi.org/10.1021/acsami.3c07081
ACS Appl. Mater. Interfaces 2023, 15, 35216−35226

Apparently, the device had good luminescence stability with no shift in EL peak position even at a high drive current (100 mA). Meanwhile, P-WLED had pure white light emission with chromaticity coordinates of (0.3134, 0.3178) (Figure 6b). Further, the device had the highest luminous efficiency at 21 mA drive current, which was around 93.98 lm/W, 76.6% higher than commercial WLED (maximum 53.27 lm/W) (Figure 6c). There were two main reasons for such high luminescence efficiency: (1) The core−shell structure effectively suppressed surface defects. (2) The wide bandgap $CsPb_2Br_5$ and narrow bandgap $CsPbBr_3$ form a quantum well structure, resulting in electrons and holes of $CsPb_2Br_5$ would be transported to conduction and valence bands of $CsPbBr_3$, increasing the radiation recombination rate.[34] Despite the higher luminous efficiency of the $CsPbX_3$ WLED (103.74 lm/W, Figure 6c), the device exhibited a tendency to decay rapidly at high drive currents, attributed to decomposition of the exposed NCs due to the rapid warming of device surfaces. Figure 6d exhibits the color rendering index (CRI) comparison of P-WLED. The results indicated that CRI of P-WLED remained above 80 at all current conditions and even reached 96 at 21 mA drive current, while the highest for $CsPbX_3$ WLED was 73 and commercial LED was 72. $CsPbBr_3$ QDs acting as light sources in P-WLEDs had narrower fwhm and released purer light, thus exhibiting better display effects.[42] Finally, the long-term operating stability of P-WLED was tested to ensure that it had practical application value. It has been known that optoelectronic devices release large amounts of thermal energy during operation, which would seriously deteriorate the optical performance of $CsPbBr_3$ QDs.[43] We recorded the surface temperature of P-LED by an infrared imager. Results showed that the temperature of the device increased to over 100 °C in 1 h of operation, and after 2 h, it stabilized at about 105 °C (Figure 6e). However, P-WLED demonstrated amazing stability; even after 24 h of continuous operation, EL intensity of green light only decayed by 2%−3%, while red light decayed by 5%−6% (Figure 6f), and these performances were absolutely superior in the face of previous reports (Table S1). In contrast, the luminescence intensity of the $CsPbX_3$ WLED decayed to 7.57% after 6 h of operation (Figure S10), demonstrating that the $CsPbBr_3$@$CsPb_2Br_5$@TiO_2 composites prepared by the double-layer passivation strategy greatly expanded applications of perovskite materials in the field of optoelectronics.

CONCLUSION

In summary, a series of uniformly sized $CsPbBr_3$@$CsPb_2Br_5$ octagonal core−shell micrometer crystals were prepared by epitaxially growing a layer of stable $CsPb_2Br_5$ shell on a $CsPbBr_3$ QDs surface by simply controlling the reaction time of thermal injection as shown in this article. Due to the passivation of surface defects by $CsPb_2Br_5$ shells, PLQY of $CsPbBr_3$ QDs was increased from 55% to 83%, and the water/thermal stability was significantly improved. Further, through hydrolysis and annealing of tetrabutyl titanate, a layer of dense TiO_2 nanoparticles was encapsulated on the $CsPbBr_3$@$CsPb_2Br_5$ surface to prepare $CsPbBr_3$@$CsPb_2Br_5$@TiO_2 composites. The $CsPbBr_3$@$CsPb_2Br_5$@TiO_2 composites exhibited excellent photocatalytic performance and recyclability benefiting from the excellent light absorption effect, efficient carrier transport performance, and unique energy band structure of the material. Meanwhile, the quasi-white LED prepared with this material had high luminous efficiency of 93.98 lm/W, and EL intensity was almost constant for 24 h of operation at over 100 °C. This provides a new perspective for future multifunctional applications of perovskite materials.

EXPERIMENTAL SECTION

Materials. Cesium carbonate (Cs_2CO_3, 99.99%), lead(II) bromide ($PbBr_2$, 99.99%), lead(II) iodide (PbI_2, 99.99%), oleic acid (OA, 85%), oleylamine (OAm, 80−90%), 1-octadecene (ODE, 90%), tetrabutyl titanate (TBOT, > 99%), and toluene (>99.7%) were purchased from Aladdin. Rhodamine B (RhB) and poly(styrene) (PS) were purchased from Macklin. The 450 nm blue light chips (5 W) and commercial WLED (5 W) were purchased from CREE, Inc. All the reagents were used without further purification.

Synthesis of $CsPbBr_3$@$CsPb_2Br_5$ Core−Shell Micrometer Crystals. Here, 2.5 mmol of Cs_2CO_3 was placed in a solution consisting of 2.5 mL of OA and 10 mL of ODE and transferred to a 100 mL three-necked flask. The solution was heated to 120 °C under vacuum and reacted for 1 h. After that, the Cs-OA precursor was obtained by heating to 140 °C and reacting for 1 h under a N_2 environment. Note that the Cs-OA precursor needs to be held at 100 °C before use.

Then, 0.3 mmol of $PbBr_2$ was placed in a solution consisting of 10 mL of ODE, 0.5 mL of OA, and 0.5 mL of OAm and transferred to another 100 mL three-necked flask. The temperature was increased to 120 °C under N_2 and held for 1 h. After that, the temperature was again increased to 150 °C for 10 min, and 0.375 mL of Cs-OA was injected into the solution (at this time, Cs^+: Pb^{2+} in the solution was 1:2). After 50 min of reaction, the three-necked flasks were immersed in ice water to the terminate reactions. The precipitates were obtained by centrifugation of the crude solution at 2000 rpm/min for 5 min and washed 2−3 times with toluene. Finally, the precipitation was dispersed into 20 mL of toluene to obtain a $CsPbBr_3$@$CsPb_2Br_5$ core−shell micrometer crystal solution.

Synthesis of $CsPbBr_3$@$CsPb_2Br_5$@TiO_2 Composites. Here, 10 μL of TBOT and 5 μL of deionized water were slowly added to the above $CsPbBr_3$@$CsPb_2Br_5$ toluene solution and stirred continuously for 3 h at room temperature for hydrolysis. After that, suspensions were centrifuged at 2000 rpm/min for 5 min to obtain a pale yellow gel-like $CsPbBr_3$@$CsPb_2Br_5$@TiO_x. The products were dried under a vacuum at 60 °C for 12 h to obtain a pale yellow $CsPbBr_3$@$CsPb_2Br_5$@TiO_x powder. Finally, the powders were annealed at 300 °C for 3 h in an Ar_2 environment (heating rate 100 °C/h) to obtain brown $CsPbBr_3$@$CsPb_2Br_5$@TiO_2 composites.

Synthesis of $CsPb(Br/I)_3$@$CsPb_2(Br/I)_5$@TiO_2 Composites by Anion Exchange Method. Here, 0.5 mmol PbI_2 (0.5 mmol) was placed in a solution consisting of 10 mL of ODE, 1 mL of OA, and 1 mL of OAm and transferred to a 100 mL three-necked flask. The temperature was increased to 120 °C for 1 h under N_2, and then, it was increased to 150 °C to continue the reaction until PbI_2 was completely dissolved. Subsequently, the flask was cooled to 60 °C to obtain the PbI_2 precursor solution. $CsPb(Br/I)_3$@$CsPb_2(Br/I)_5$ core−shell micrometer crystals were obtained by dropping 1 mL of PbI_2 precursor into $CsPbBr_3$@$CsPb_2Br_5$ toluene solution and washing with the same procedure after 10 min of reaction. Finally, the process of encapsulating TiO_2 nanoparticles was the same as before except that $CsPbBr_3$@$CsPb_2Br_5$ was replaced with $CsPb(Br/I)_3$@$CsPb_2(Br/I)_5$.

Preparation of Quasi-Perovskite White Light-Emitting Diodes (P-WLED). Here, 0.1 g of $CsPbBr_3$@$CsPb_2Br_5$@TiO_2 powders and 0.5 g of PS particles were placed in 10 mL of toluene and stirred at 60 °C for 3 h. Then, the solution was poured into prefabricated molds, and $CsPbBr_3$@$CsPb_2Br_5$@TiO_2 polymer films were deposited at room temperature. The $CsPb(Br/I)_3$@$CsPb_2(Br/I)_5$@TiO_2 polymer films were prepared in a similar process by replacing $CsPbBr_3$@$CsPb_2Br_5$@TiO_2 with $CsPb(Br/I)_3$@$CsPb_2(Br/I)_5$@TiO_2. Finally, the two films were covered on a 450 nm blue light chip to obtain P-WLED.

Characterization Methods. The morphology and microstructure of the samples were analyzed by HRTEM (JEOL JEM-F200). The

https://doi.org/10.1021/acsami.3c07081
ACS Appl. Mater. Interfaces 2023, 15, 35216−35226

EDS spectra of samples were studied with a field emission scanning electron microscope (FESEM, FEI Quatan FEG 250) equipped with an energy dispersive spectrometer (EDS). Photoluminescence (PL) spectra and time-resolved PL (TRPL) decay curves of samples were recorded on an Edinburgh Instruments FLS1000 spectrometer. The ultraviolet−visible (UV−vis) absorption spectra were recorded with a Jasco V-570 UV/vis/NIR spectrophotometer. All test samples for fluorescence and absorption spectra were taken as 0.01 g of powder in 10 mL of toluene and sonicated for 20 min. X-ray diffraction (XRD) patterns of samples were obtained with a DB-ADVANCE X-ray diffractometer. The photocurrent response of samples was recorded with an electrochemical workstation (CHI600E, Shanghai Chenhua) and a 500 W Xe lamp with AM 1.5 G filter. The electroluminescence (EL) spectra, luminous efficiency, color rendering index, and chromaticity coordinate of WLED were obtained with a Keithley 2400 light meter and Photo Research 670 spectrometer. The P-LED surface temperature was detected and recorded using a thermal infrared imager (FOTRIC, USA).

■ ASSOCIATED CONTENT

Supporting Information

The Supporting Information is available free of charge at https://pubs.acs.org/doi/10.1021/acsami.3c07081.

TEM and XRD patterns of the samples at different reaction times; EDS spectra, SEM, and optical photographs of the samples; comparison of absorption spectra and catalytic performance of different catalysts; optical band gap of the sample; cyclic catalytic stability of $CsPbBr_3$@$CsPb_2Br_5$@TiO_2; SEM images of samples prepared by anion exchange; operating stability of $CsPbX_3$ WLEDs; and comparison of the performance of this work with previous related reports (PDF)

■ AUTHOR INFORMATION

Corresponding Author

Minqiang Wang − *Electronic Materials Research Laboratory, Key Laboratory of the Ministry of Education International Center for Dielectric Research, Shannxi Engineering Research Center of Advanced Energy Materials and Devices, Xi'an Jiaotong University, 710049 Xi'an, China*; Email: mqwang@xjtu.edu.cn

Authors

Chen Zhang − *Electronic Materials Research Laboratory, Key Laboratory of the Ministry of Education International Center for Dielectric Research, Shannxi Engineering Research Center of Advanced Energy Materials and Devices, Xi'an Jiaotong University, 710049 Xi'an, China*; orcid.org/0009-0006-2744-2513

Zeyu Wang − *John A. Paulson School of Engineering and Applied Sciences, Harvard University, Canbridge, Massachusetts 02138, United States*

Jindou Shi − *Electronic Materials Research Laboratory, Key Laboratory of the Ministry of Education International Center for Dielectric Research, Shannxi Engineering Research Center of Advanced Energy Materials and Devices, Xi'an Jiaotong University, 710049 Xi'an, China*; orcid.org/0000-0003-1082-5009

Junnan Wang − *Electronic Materials Research Laboratory, Key Laboratory of the Ministry of Education International Center for Dielectric Research, Shannxi Engineering Research Center of Advanced Energy Materials and Devices, Xi'an Jiaotong University, 710049 Xi'an, China*; orcid.org/0000-0002-3074-0195

Zheyuan Da − *Electronic Materials Research Laboratory, Key Laboratory of the Ministry of Education International Center for Dielectric Research, Shannxi Engineering Research Center of Advanced Energy Materials and Devices, Xi'an Jiaotong University, 710049 Xi'an, China*

Yun Zhou − *Electronic Materials Research Laboratory, Key Laboratory of the Ministry of Education International Center for Dielectric Research, Shannxi Engineering Research Center of Advanced Energy Materials and Devices, Xi'an Jiaotong University, 710049 Xi'an, China*

Youlong Xu − *Electronic Materials Research Laboratory, Key Laboratory of the Ministry of Education International Center for Dielectric Research, Shannxi Engineering Research Center of Advanced Energy Materials and Devices, Xi'an Jiaotong University, 710049 Xi'an, China*

Nikolai V. Gaponenko − *Belarusian State University of Informatics and Radioelectronics, 220013 Minsk, Belarus*

Arshad Saleem Bhatti − *Centre for Micro and Nano Devices, Department of Physics, COMSATS Institute of Information Technology, Islamabad 44500, Pakistan*

Complete contact information is available at: https://pubs.acs.org/10.1021/acsami.3c07081

Notes

The authors declare no competing financial interest.

■ ACKNOWLEDGMENTS

This work was supported by the National Natural Science Foundation of China (NSFC, 52161145103 and 61774124), National Key R&D Program of China (2022YFE0122500 and 2019YFB1503200), 111 Program (B14040), and Shaanxi Provincial Key Research and Development Program (2021GXLH-Z-084). The authors thank Ms. Dan He at the Instrument Anaysis Center of Xi'an Jiaotong University for her help with the time-resolved PL analysis.

■ REFERENCES

(1) Duan, L.; Hu, L.; Guan, X.; Lin, C. H.; Chu, D.; Huang, S.; Liu, X.; Yuan, J.; Wu, T. Quantum Dots for Photovoltaics: A Tale of Two Materials. *Adv. Energy Mater.* **2021**, *11* (20).2100354

(2) Protesescu, L.; Yakunin, S.; Bodnarchuk, M. I.; Krieg, F.; Caputo, R.; Hendon, C. H.; Yang, R. X.; Walsh, A.; Kovalenko, M. V. Nanocrystals of Cesium Lead Halide Perovskites ($CsPbX_3$, X = Cl, Br, and I): Novel Optoelectronic Materials Showing Bright Emission with Wide Color Gamut. *Nano Lett.* **2015**, *15* (6), 3692−6.

(3) Cottingham, P.; Brutchey, R. L. On the Crystal Structure of Colloidally Prepared $CsPbBr_3$ Quantum Dots. *Chem. Commun. (Camb)* **2016**, *52* (30), 5246−9.

(4) Eperon, G. E.; Paternò, G. M.; Sutton, R. J.; Zampetti, A.; Haghighirad, A. A.; Cacialli, F.; Snaith, H. J. Inorganic Caesium Lead Iodide Perovskite Solar Cells. *Journal of Materials Chemistry A* **2015**, *3* (39), 19688−19695.

(5) Cheng, R.; Steele, J. A.; Roeffaers, M. B. J.; Hofkens, J.; Debroye, E. Dual-Channel Charge Carrier Transfer in $CsPbX_3$ Perovskite/$W_{18}O_{49}$ Composites for Selective Photocatalytic Benzyl Alcohol Oxidation. *ACS Applied Energy Materials* **2021**, *4* (4), 3460−3468.

(6) Hou, J.; Cao, S.; Wu, Y.; Gao, Z.; Liang, F.; Sun, Y.; Lin, Z.; Sun, L. Inorganic Colloidal Perovskite Quantum Dots for Robust Solar CO_2 Reduction. *Chemistry* **2017**, *23* (40), 9481−9485.

(7) Dong, Y.; Wang, Y. K.; Yuan, F.; Johnston, A.; Liu, Y.; Ma, D.; Choi, M. J.; Chen, B.; Chekini, M.; Baek, S. W.; Sagar, L. K.; Fan, J.; Hou, Y.; Wu, M.; Lee, S.; Sun, B.; Hoogland, S.; Quintero-Bermudez, R.; Ebe, H.; Todorovic, P.; Dinic, F.; Li, P.; Kung, H. T.; Saidaminov, M. I.; Kumacheva, E.; Spiecker, E.; Liao, L. S.; Voznyy, O.; Lu, Z. H.; Sargent, E. H. Bipolar-Shell Resurfacing for Blue LEDs based on

Strongly Confined Perovskite Quantum Dots. *Nat. Nanotechnol* **2020**, *15* (8), 668−674.
(8) Song, J.; Li, J.; Li, X.; Xu, L.; Dong, Y.; Zeng, H. Quantum Dot Light-Emitting Diodes Based on Inorganic Perovskite Cesium Lead Halides ($CsPbX_3$). *Adv. Mater.* **2015**, *27* (44), 7162−7.
(9) Lin, K.; Xing, J.; Quan, L. N.; de Arquer, F. P. G.; Gong, X.; Lu, J.; Xie, L.; Zhao, W.; Zhang, D.; Yan, C.; Li, W.; Liu, X.; Lu, Y.; Kirman, J.; Sargent, E. H.; Xiong, Q.; Wei, Z. Perovskite Light-Emitting Diodes with External Quantum Efficiency Exceeding 20%. *Nature* **2018**, *562* (7726), 245−248.
(10) Yu, Y.; Liang, Y.; Yong, J.; Li, T.; Hossain, M. S.; Liu, Y.; Hu, Y.; Ganesan, K.; Skafidas, E. Low-Temperature Solution-Processed Transparent QLED Using Inorganic Metal Oxide Carrier Transport Layers. *Adv. Funct. Mater.* **2022**, *32* (3), 2106387.
(11) Pan, J.; Shang, Y.; Yin, J.; De Bastiani, M.; Peng, W.; Dursun, I.; Sinatra, L.; El-Zohry, A. M.; Hedhili, M. N.; Emwas, A. H.; Mohammed, O. F.; Ning, Z.; Bakr, O. M. Bidentate Ligand-Passivated $CsPbI_3$ Perovskite Nanocrystals for Stable Near-Unity Photoluminescence Quantum Yield and Efficient Red Light-Emitting Diodes. *J. Am. Chem. Soc.* **2018**, *140* (2), 562−565.
(12) Zhong, Q.; Cao, M.; Hu, H.; Yang, D.; Chen, M.; Li, P.; Wu, L.; Zhang, Q. One-Pot Synthesis of Highly Stable $CsPbBr_3$@SiO_2 Core-Shell Nanoparticles. *ACS Nano* **2018**, *12* (8), 8579−8587.
(13) Vighnesh, K.; Wang, S.; Liu, H.; Rogach, A. L. Hot-Injection Synthesis Protocol for Green-Emitting Cesium Lead Bromide Perovskite Nanocrystals. *ACS Nano* **2022**, *16* (12), 19618−19625.
(14) Shi, J.; Ge, W.; Gao, W.; Xu, M.; Zhu, J.; Li, Y. Enhanced Thermal Stability of Halide Perovskite $CsPbX_3$ Nanocrystals by a Facile TPU Encapsulation. *Advanced Optical Materials* **2020**, *8* (4), 1901516.
(15) Guggisberg, D.; Yakunin, S.; Neff, C.; Aebli, M.; Gunther, D.; Kovalenko, M. V.; Dirin, D. N. Colloidal $CsPbX_3$ Nanocrystals with Thin Metal Oxide Gel Coatings. *Chem. Mater.* **2023**, *35* (7), 2827−2834.
(16) Fan, M.; Huang, J.; Turyanska, L.; Bian, Z.; Wang, L.; Xu, C.; Liu, N.; Li, H.; Zhang, X.; Zhang, C.; Yang, X. Efficient All-Perovskite White Light-Emitting Diodes Made of In Situ Grown Perovskite-Mesoporous Silica Nanocomposites. *Adv. Funct. Mater.* **2023**, *33*, 2215032.
(17) Shi, J.; Ge, W.; Tian, Y.; Xu, M.; Gao, W.; Wu, Y. Enhanced Stability of All-Inorganic Perovskite Light-Emitting Diodes by a Facile Liquid Annealing Strategy. *Small* **2021**, *17* (14), No. 2006568.
(18) Jiang, G.; Guhrenz, C.; Kirch, A.; Sonntag, L.; Bauer, C.; Fan, X.; Wang, J.; Reineke, S.; Gaponik, N.; Eychmuller, A. Highly Luminescent and Water-Resistant $CsPbBr_3$-$CsPb_2Br_5$ Perovskite Nanocrystals Coordinated with Partially Hydrolyzed Poly(methyl methacrylate) and Polyethylenimine. *ACS Nano* **2019**, *13* (9), 10386−10396.
(19) Baek, K. Y.; Lee, W.; Lee, J.; Kim, J.; Ahn, H.; Kim, J. I.; Kim, J.; Lim, H.; Shin, J.; Ko, Y. J.; Lee, H. D.; Friend, R. H.; Lee, T. W.; Lee, J.; Kang, K.; Lee, T. Mechanochemistry-driven Engineering of 0D/3D Heterostructure for Designing Highly Luminescent Cs-Pb-Br Perovskites. *Nat. Commun.* **2022**, *13* (1), 4263.
(20) Li, Z. J.; Hofman, E.; Li, J.; Davis, A. H.; Tung, C. H.; Wu, L. Z.; Zheng, W. Photoelectrochemically Active and Environmentally Stable $CsPbBr_3$/TiO_2 Core/Shell Nanocrystals. *Adv. Funct. Mater.* **2018**, *28* (1), 1704288.
(21) Ruan, L.; Zhang, Y. NIR-Excitable Heterostructured Upconversion Perovskite Nanodots with Improved Stability. *Nat. Commun.* **2021**, *12* (1), 219.
(22) Ruan, L. J.; Tang, B.; Ma, Y. Improving the Stability of $CsPbBr_3$ Nanocrystals in Ethanol by Capping with $PbBr_2$-Adlayers. *J. Phys. Chem. C* **2019**, *123* (18), 11959−11967.
(23) Xie, K.; Wei, S.; Alhadhrami, A.; Liu, J.; Zhang, P.; Elnaggar, A. Y.; Zhang, F.; Mahmoud, M. H. H.; Murugadoss, V.; El-Bahy, S. M.; Wang, F.; Li, C.; Li, G. Synthesis of $CsPbBr_3$/$CsPb_2Br_5$@Silica Yolk-Shell Composite Microspheres: Precisely Controllable Structure and Improved Catalytic Activity for Dye Degradation. *Advanced Composites and Hybrid Materials* **2022**, *5* (2), 1423−1432.
(24) Tong, Y.; Wang, Q.; Mei, E.; Liang, X.; Gao, W.; Xiang, W. One-Pot Synthesis of $CsPbX_3$ (X = Cl, Br, I) @Zeolite: A Potential Material for Wide-Color-Gamut Backlit Displays and Upconversion Emission. *Advanced Optical Materials* **2021**, *9* (11), 2100012.
(25) He, M.; Zhang, Q.; Carulli, F.; Erroi, A.; Wei, W.; Kong, L.; Yuan, C.; Wan, Q.; Liu, M.; Liao, X.; Zhan, W.; Han, L.; Guo, X.; Brovelli, S.; Li, L. Ultra-stable, Solution-Processable $CsPbBr_3$-SiO_2 Nanospheres for Highly Efficient Color Conversion in Micro Light-Emitting Diodes. *ACS Energy Letters* **2023**, *8* (1), 151−158.
(26) Shao, G.; Zhao, Y.; Yu, Y.; Yang, H.; Liu, X.; Zhang, Y.; Xiang, W.; Liang, X. Bright emission and High Photoluminescence $CsPb_2Br_5$ NCs Encapsulated in Mesoporous Silica with Ultrahigh Stability and Excellent Optical Properties for White Light-emitting Diodes. *Journal of Materials Chemistry C* **2019**, *7* (43), 13585−13593.
(27) Jang, E.; Jang, H. Review: Quantum Dot Light-Emitting Diodes. *Chem. Rev.* **2023**, *123* (8), 4663−4692.
(28) Shi, J.; Wang, M.; Zhang, C.; Wang, J.; Zhou, Y.; Xu, Y.; Gaponenko, N. V. Enhanced Stability of Lead-Free Double Perovskite $Cs_2Na_{1-x}Bi_{1-x}Mn_{2x}Cl_6$ Microcrystals and Their Optoelectronic Devices under High Humidity Environment by SiO_2 Encapsulation. *Materials Today Chemistry* **2023**, *29*, 101480.
(29) Balakrishnan, S. K.; Kamat, P. V. Ligand Assisted Transformation of Cubic $CsPbBr_3$ Nanocrystals into Two-Dimensional $CsPb_2Br_5$ Nanosheets. *Chem. Mater.* **2018**, *30* (1), 74−78.
(30) Huang, Z. P.; Ma, B.; Wang, H.; Li, N.; Liu, R. T.; Zhang, Z. Q.; Zhang, X. D.; Zhao, J. H.; Zheng, P. Z.; Wang, Q.; Zhang, H. L. In Situ Growth of 3D/2D ($CsPbBr_3$/$CsPb_2Br_5$) Perovskite Heterojunctions toward Optoelectronic Devices. *J. Phys. Chem. Lett.* **2020**, *11* (15), 6007−6015.
(31) Zhang, X.; Xu, B.; Zhang, J.; Gao, Y.; Zheng, Y.; Wang, K.; Sun, X. W. All-Inorganic Perovskite Nanocrystals for High-Efficiency Light Emitting Diodes: Dual-Phase $CsPbBr_3$-$CsPb_2Br_5$ Composites. *Adv. Funct. Mater.* **2016**, *26* (25), 4595−4600.
(32) Wang, K. H.; Wu, L.; Li, L.; Yao, H. B.; Qian, H. S.; Yu, S. H. Large-Scale Synthesis of Highly Luminescent Perovskite-Related $CsPb_2Br_5$ Nanoplatelets and Their Fast Anion Exchange. *Angew. Chem., Int. Ed. Engl.* **2016**, *55* (29), 8328−32.
(33) Li, G.; Wang, H.; Zhu, Z.; Chang, Y.; Zhang, T.; Song, Z.; Jiang, Y. Shape and Phase Evolution from $CsPbBr_3$ Perovskite Nanocubes to Tetragonal $CsPb_2Br_5$ Nanosheets with an Indirect Bandgap. *Chem. Commun. (Camb)* **2016**, *52* (75), 11296−11299.
(34) Qiao, B.; Song, P.; Cao, J.; Zhao, S.; Shen, Z.; Di, G.; Liang, Z.; Xu, Z.; Song, D.; Xu, X. Water-Resistant, Monodispersed and Stably Luminescent $CsPbBr_3$/$CsPb_2Br_5$ Core-Shell-Like Structure Lead Halide Perovskite Nanocrystals. *Nanotechnology* **2017**, *28* (44), 445602.
(35) Han, C.; Li, C.; Zang, Z.; Wang, M.; Sun, K.; Tang, X.; Du, J. Tunable Luminescent $CsPb_2Br_5$ Nanoplatelets: Applications in Light-Emitting Diodes and Photodetectors. *Photonics Research* **2017**, *5* (5), 473.
(36) He, Y.; Tilocca, A.; Dulub, O.; Selloni, A.; Diebold, U. Local Ordering and Electronic Signatures of Submonolayer Water on Anatase TiO_2(101). *Nat. Mater.* **2009**, *8* (7), 585−9.
(37) Chang, M.; Song, Y.; Chen, J.; Cui, L.; Shi, Z.; Sheng, Y.; Zou, H. Photocatalytic and Photoluminescence Properties of Core-Shell SiO_2@TiO_2:Eu^{3+},Sm^{3+} and Its Etching Products. *ACS Sustainable Chem. Eng.* **2018**, *6* (1), 223−236.
(38) Ding, L.; Borjigin, B.; Li, Y.; Yang, X.; Wang, X.; Li, H. Assembling an Affinal 0D $CsPbBr_3$/2D $CsPb_2Br_5$ Architecture by Synchronously In Situ Growing $CsPbBr_3$ QDs and $CsPb_2Br_5$ Nanosheets: Enhanced Activity and Reusability for Photocatalytic CO_2 Reduction. *ACS Appl. Mater. Interfaces* **2021**, *13* (43), 51161−51173.
(39) Liang, T.; Liu, W.; Liu, X.; Li, Y.; Wu, W.; Fan, J. In Situ Phase-Transition Crystallization of All-Inorganic Water-Resistant Exciton-Radiative Heteroepitaxial $CsPbBr_3$-$CsPb_2Br_5$ Core-Shell Perovskite Nanocrystals. *Chem. Mater.* **2021**, *33* (13), 4948−4959.
(40) Zhu, W.; Xia, Z.; Shi, B.; Lü, C. Water-Triggered Conversion of Cs_4PbBr_6@TiO_2 into Cs_4PbBr_6/$CsPbBr_3$@TiO_2 Three-Phase Heter-

https://doi.org/10.1021/acsami.3c07081
ACS Appl. Mater. Interfaces 2023, 15, 35216−35226

ojunction for Enhanced Visible-Light-Driven Photocatalytic Degradation of Organic Pollutants. *Materials Today Chemistry* **2022**, *24*, 100880.
(41) Chen, S.; Cao, W.; Liu, T.; Tsang, S. W.; Yang, Y.; Yan, X.; Qian, L. On the Degradation Mechanisms of Quantum-Dot Light-Emitting Diodes. *Nat. Commun.* **2019**, *10* (1), 765.
(42) Ye, Z. T.; Wu, J. Y. Use of Recycling-Reflection Color-Purity Enhancement Film to Improve Color Purity of Full-Color Micro-LEDs. *Nanoscale Res. Lett.* **2022**, *17* (1), 1.
(43) Wang, S.; Wang, H.; Zhang, D.; Dou, Y.; Li, W.; Cao, F.; Yin, L.; Wang, L.; Zhang, Z.-J.; Zhang, J.; Yang, X. Perovskite Nanocrystals-Polymer Composites with a Micro/Nano Structured Superhydrophobic Surface for Stable and Efficient White Light-Emitting Diodes. *Chemical Engineering Journal* **2022**, *437*, 135303.
(44) Ravi, V. K.; Saikia, S.; Yadav, S.; Nawale, V. V.; Nag, A. $CsPbBr_3$/ZnS Core/Shell Type Nanocrystals for Enhancing Luminescence Lifetime and Water Stability. *ACS Energy Letters* **2020**, *5* (6), 1794−1796.

https://doi.org/10.1021/acsami.3c07081
ACS Appl. Mater. Interfaces 2023, 15, 35216−35226